npj | 2D materials and applications

Article

Published in partnership with FCT NOVA with the support of E-MRS

https://doi.org/10.1038/s41699-024-00503-7

Optical control of multiple resistance levels in graphene for memristic applications

Harsimran Kaur Mann[1], Mainak Mondal[1], Vivek Sah[1], Kenji Watanabe[2], Takashi Taniguchi[3], Akshay Singh[1] ✉ & Aveek Bid[1] ✉

Neuromorphic computing has emphasized the need for memristors with non-volatile, multiple conductance levels. This paper demonstrates the potential of hexagonal boron nitride (hBN)/graphene heterostructures to act as memristors with multiple resistance states that can be optically tuned using visible light. The number of resistance levels in graphene can be controlled by modulating doping levels, achieved by varying the electric field strength or adjusting the duration of optical illumination. Our measurements show that this photodoping of graphene results from the optical excitation of charge carriers from the nitrogen-vacancy levels of hBN to its conduction band, with these carriers then being transferred to graphene by the gate-induced electric field. We develop a qualitative model to describe our observations. Additionally, utilizing our device architecture, we propose a memristive crossbar array for vector-matrix multiplications.

Neuromorphic computing (NC), inspired by the human brain, has emerged as a new paradigm beyond von Neumann computing. NC provides a low-energy alternative to the traditional von Neumann architectures, promoting sustainable computation in our modern information age. The critical hardware building blocks for NC are memristors (artificial synapse), neural processing units, and threshold switches (artificial neurons)[1–5]. A memristor is a fundamental electronic component whose resistance is dependent on the charge that has flown through it; it is a resistor with a memory. This charge-history dependence of resistance can be exploited in machine learning frameworks where computation can be carried out via cross-bar arrays, and synaptic weights (such as weights for neural networks) can be modified by a certain number of electrical pulses, leading to in-memory computing. A low-power, non-volatile memristor is essential to exploit NC's benefits fully.

A prerequisite for memristic action is a platform with non-volatile doping. Chemical and electrostatic doping are the two most commonly used techniques to induce charge carriers in 2-D channels. Chemical doping is done by hetero-atom substitution and adsorption of molecular adsorbates onto graphene and other 2D materials. There are several drawbacks of this approach, including limited control over doping concentration, introduction of uncontrolled structural defects and lattice strains, unintentional impurity introduction, challenges in maintaining stability and diffusion control, and the sensitivity of the sample to processing conditions[6–14].

Electrostatic doping involves doping using an external local gate. While this technique avoids most of the disadvantages of chemical doping listed above, the magnitude of doping attainable is limited by the breakdown voltage of the gate dielectric[15–18]. Liquid ionic gating has the potential of reaching higher doping levels than is achievable by dielectric gates but at the cost of device instability and non-scalability[19,20].

A viable alternative is optical doping of graphene on hexagonal boron nitride (hBN) substrates[21–36]. hBN has a band gap of 6 eV with several intermediate defect states that can be optically excited[37–40]. This method involves the controlled optical excitation of charge carriers from defect states of hBN and their transfer to graphene using an external electric field. This technique is reversible without adversely affecting transport mobility and defect density.

In this article, we present an in-depth study of optical doping in hBN/graphene heterostructures using visible light. Our research reveals that electrons in the nitrogen-vacancy defect state in hBN can be optically excited with violet light and transferred to graphene through electrostatic gating. This technique enables high-density doping of graphene, with the doping level controlled by gate voltage or illumination time. The dynamics of this doping process, measured with millisecond temporal resolution, can be adjusted by varying the illumination wavelength and optical power. Furthermore, we demonstrate that a graphene/hBN heterostructure can function as a memristor, exhibiting multiple resistance levels. The device's

[1]Department of Physics, Indian Institute of Science, Bangalore, 560012, India. [2]Research Center for Electronic and Optical Materials, National Institute for Materials Science, 1-1 Namiki, Tsukuba, 305-0044, Japan. [3]Research Center for Materials Nanoarchitectonics, National Institute for Materials Science, 1-1 Namiki, Tsukuba, 305-0044, Japan. ✉e-mail: aksy@iisc.ac.in; aveek@iisc.ac.in

compact structure and room-temperature operation enhance its potential for scalable, room-temperature neuromorphic applications.

Results and discussion

Single-layer graphene devices encapsulated between thin hBN crystals were fabricated using the dry transfer method. 1-D electrical contacts to the graphene were achieved by lithography and dry etching, followed by Cr/Au metallization (Fig. 1a)[41]. A back-gate voltage, V_g, tuned the charge carrier number density. Electrical transport measurements were performed using a low-frequency AC measurement technique. The Dirac point (maxima in the device resistance R) is attained at $V_g = 0$ V (Fig. 1b), solid blue line, attesting to the absence of charged impurities in the graphene channel.

Optoelectronic measurements

The optoelectronic measurements were carried out at room temperature, and the sample was illuminated by using either an LED of wavelength, $\lambda = 427$ m or a Ti Sapphire pulsed laser (80 MHz repetition rate, 100 fs pulse width). To photo-dope the device, we use the following protocol: The gate voltage is set to a desired value V_g^*, and the device is exposed to the light of wavelength 427 nm of intensity $I = 62$ Wm^{-2}, till the resistance saturates to its value at the Dirac point, R_{DP} (Fig. 1c). The light is turned off at this point, and the gate response of the device is measured. It was found that the entire $R - V_g$ plot shifts with the Dirac point at V_g^* (Fig. 1b—solid red line; in this example $V_g^* = -3$ V), establishing that the device is now electron-doped. We refer to this step as the SET protocol wherein the Dirac point can be set deterministically at any desired value of V_g. To RESET the device, it is exposed to a higher light intensity $I = 458$ Wm^{-2} at $V_g^* = 0$ V until the Dirac point shifts to $V_g = 0$ V. This protocol brings the Dirac point of the device back to $V_g = 0$ V (Fig. 1b—dotted green line). As illustrated in Fig. 1b, the process can be repeated without degradation in the device characteristics.

Figure 1 (d) shows snapshots of the $R - V_g$ data in 10 s intervals during the SET process. During this measurement, the light was turned on for 10 s with $V_g^* = -2$ V. The illumination was turned off, and the $R - V_g$ curve was measured. The process is repeated multiple times to generate the plots in Fig. 1d. The intensity of the light was kept very low ($I = 4$ Wm^{-2}) to allow for a much slower rate of resistance change. One can see that the entire transfer curve shifts gradually to the left until the Dirac point reaches $V_g^* = -2$ V. The results for similar measurements done with different values of V_g^* are shown in Fig. 1e. These measurements establish that the Dirac point can be moved deterministically to any value of the gate voltage either by controlling the exposure time (Fig. 1d) or the value of V_g^* at which the device is illuminated (Fig. 1e). The detailed temporal dynamics of R during the entire 'SET-RESET' process are discussed in Supplementary Note 3.

After setting up the SET/RESET protocol, we now show that the resistance of the sample at a specific gate voltage can be repeatedly alternated between two distinct states (Fig. 2a). The data for a single light pulse is shown in Fig. 2b, which shows the saturation in the two states, hence the stability of the SET and RESET states. Moreover, adjusting the light exposure time makes switching between multiple resistance values possible, as depicted in Fig. 2c. In this measurement, the light was turned on for 10 s (blue shaded region of the timeline), during which R increased. The light was then turned off. The value of R was stable at the value it reached when the illumination was cut off. This process can be repeated to produce multiple stable resistance levels in graphene.

Figure 2d, e shows controlled switching between multiple resistance states in an arbitrary and on-demand manner, demonstrating stability and repeatability in the resistance states. The maximum fluctuations measured in the resistance around the resistance states for repeated switching was found to be $\pm 0.05 \times R/R_{DP}$ (Supplementary Note 6). This on-demand switching, stability and repeatability is a key indicator for the robustness of the device for memristor application.

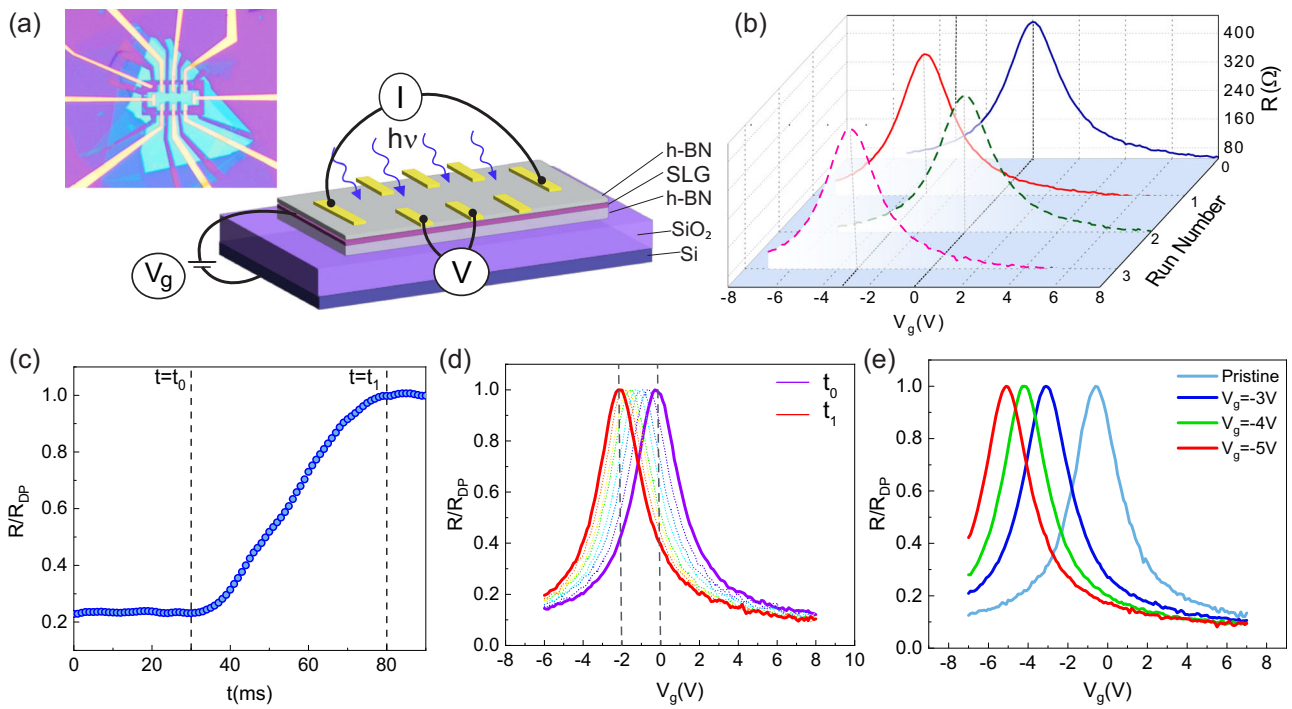

Fig. 1 | Device characteristics and optical doping. a Optical image of the device and a schematic of the device structure. **b** Longitudinal resistance as a function of gate voltage for the pristine sample before illumination (blue solid line), after photodoping at $V_g^* = -3$ V (red solid line), after erasing the doping (green dotted line), and after photodoping again at $V_g^* = -3$ V (pink dotted line). **c** Change in the longitudinal R as a function of time for constant power and gate voltage on exposure to light. $t = t_0$ marks when the light was turned on and $t = t_1$ when the light was turned off. **d** Snapshots of $R - V_g$ plots as the Dirac point progressively shifts from $V_g = 0$ V at $t = t_0$ (solid purple line) to $V_g^* = -2$ V at $t = t_1$ (solid red line). **e** Representative plots of deterministic shifting of the Dirac point to desired values of V_g by photodoping. R_{DP} is the four-probe resistance at the Dirac point.

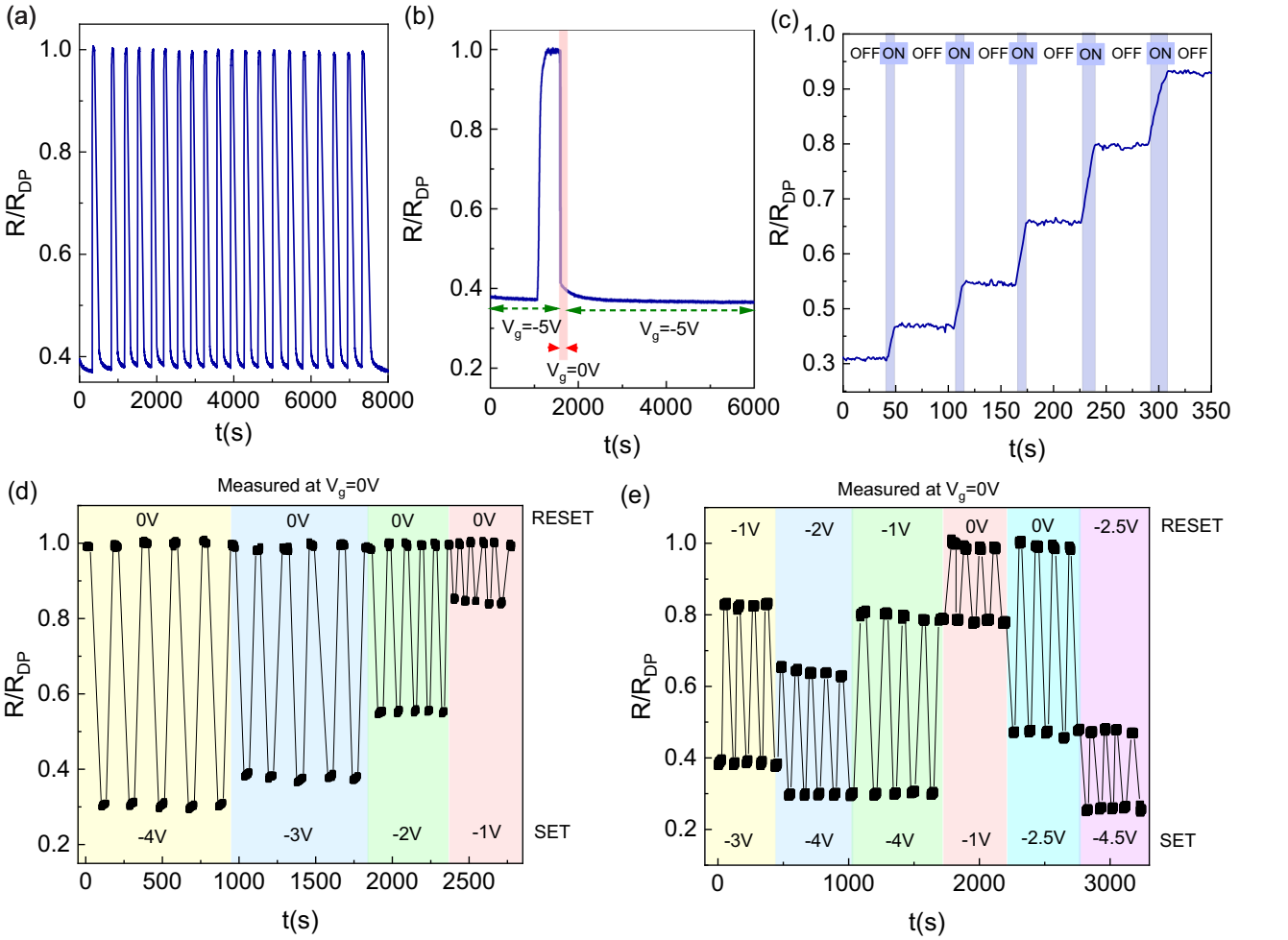

Fig. 2 | Reproducible multiple states. a Optical switching of the device's resistance between two well-defined values at $V_g^* = -5V$ with LED light source of $\lambda = 427$ nm and I = 62 Wm^{-2}. **b** Resistance versus time graph for a single light pulse of SET and RESET. **c** Figure illustrating optical pinning of R to multiple values. The blue shaded region marks when the light was switched on (hence R increased with t). The white regions show the time the light was off. LED light source of $\lambda = 427$ nm and I = 4 Wm^{-2} was used with $V_g^* = -5$ V. For **a**–**c** the R/R_{DP} values are recorded at $V_g^* = -5$ V. **d** Successive optical switching of the device's resistance between two well-defined levels; SET level at $V_g^* = -4$ V, −3 V, −2 V, −1 V and RESET level $V_g^* = 0$ V. **e** Optical switching of the device's resistance between different distinct resistance levels, defined by V_g^*. For both (**d**) and (**e**), the measurements were done with an LED light source of $\lambda = 427$ nm. The intensity of illumination was $I = 62$ Wm^{-2} for SET and $I = 458$ Wm^{-2} for RESET. The R/R_{DP} value is measured at $V_g^* = 0$ V.

Fig. 3 | Memristor. a Schematic of the proposed cross bar geometric memristor. **b** Schematic of the individual device forming a cell of the memristor.

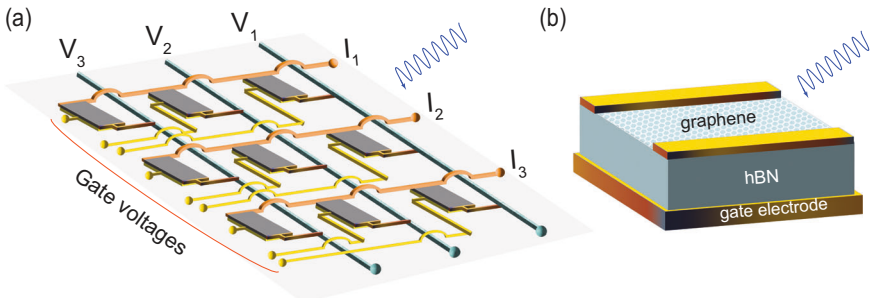

Application as memristor

As shown in Fig. 2c, our device has at least six stable resistance states, with more resistance states also accessible by lower optical powers. Such an hBN/graphene heterostructure with multiple stable resistance values holds significant potential for developing memristor devices for vector-matrix multiplication and machine learning (ML) applications[42–45]. Several such devices can be fabricated in a cross-bar array for a typical linear algebra calculation, with voltages as inputs and currents as outputs. A new vector-matrix multiplication operation can be carried out by modifying the weights of each cross-bar intersection, i.e., by changing the resistance of the channels. For hardware implementation of ML training, the synaptic weights of a neural layer (each layer will be a separate cross-bar array) can be similarly modified.

We propose a cross-bar geometry schematically shown in Fig. 3a to achieve the above objectives. Its compact footprint offers distinct advantages over other structures. Each device unit (shown schematically in Fig. 3b) is individually gated; this architecture is conveniently achievable using

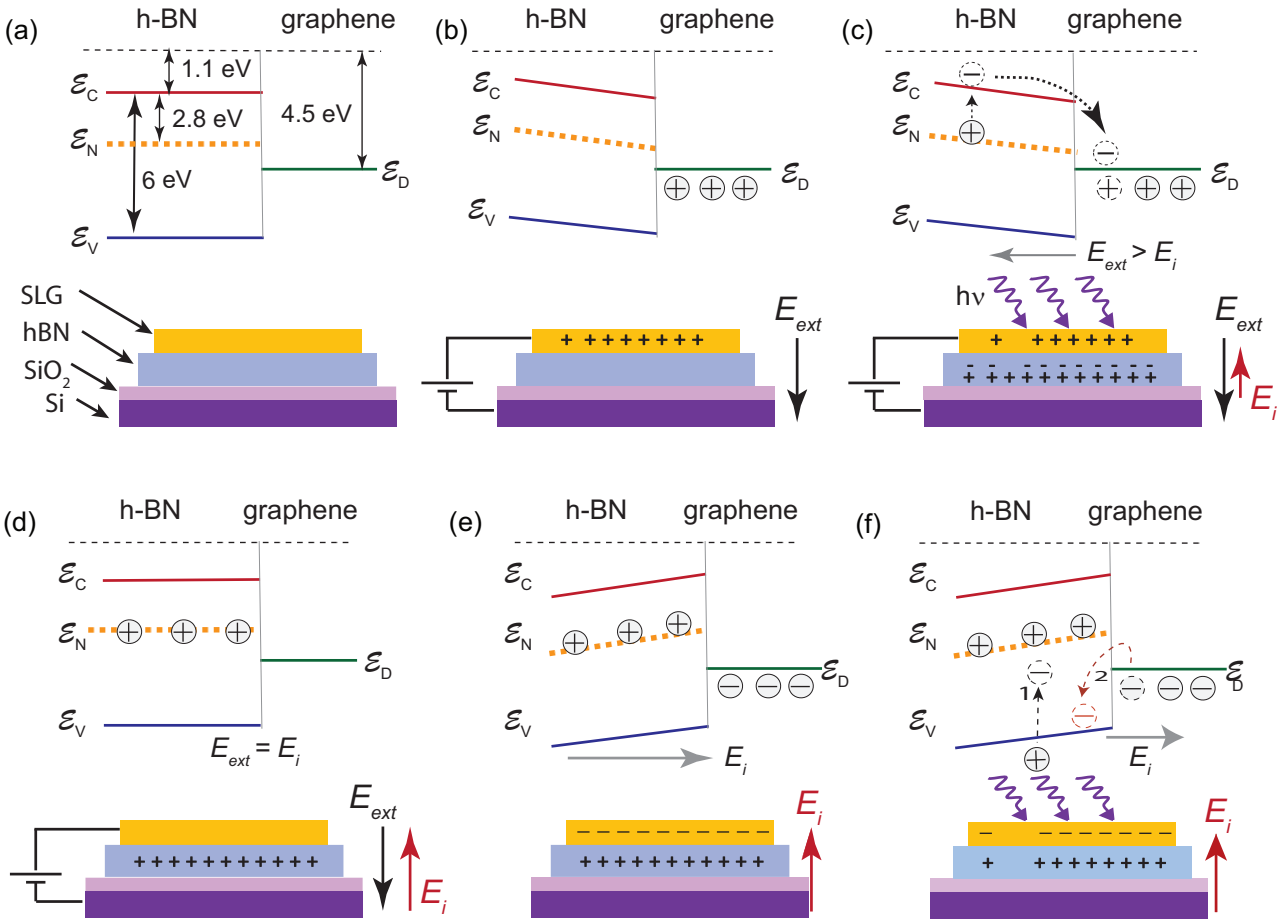

Fig. 4 | Schematic energy band alignment (top panels) and charge distribution (bottom panels) in the device under different conditions. $\mathcal{E}_C$, $\mathcal{E}_N$ and $\mathcal{E}_V$ represent the conduction band edge, N-vacancy mid-gap state and valence band edge of hBN, respectively. a For $V_g^* = 0, h\nu = 0$, hBN and graphene are charge neutral. **b** The graphene channel acquires a positive charge for V_g^*<0 and $h\nu = 0$. The resultant electric field E_{ext} bends the bands of the hBN. **c** SET: For V_g^*<0 and $h\nu \neq 0$, electrons are transferred from $\mathcal{E}_N$ (orange dotted line) to $\mathcal{E}_C$ (solid red line) of hBN. These electrons drift into graphene (represented by the dotted electrons) and reduce its net positive charge. **d** The doping process stops when $E_i = E_{ext}$. The hBN bands flatten out, graphene is charge neutral, and the hBN is left positively charged. **e** After the gate voltage is set to zero, graphene draws a net negative charge from the contacts, making it electron-doped and the total system charge neutral. (**f**) RESET: For $V_g^* = 0$ V and $h\nu \neq 0$, electrons are excited from $\mathcal{E}_v$ (blue solid line) of the hBN to recombine with the holes in $\mathcal{E}_N$ (orange dotted line). The electrons from graphene (represented by the red dotted circles) drift into hBN $\mathcal{E}_v$ and recombine with the holes left behind.

modern nano-fabrication processes. Before each operation, the channel resistance of each device is SET by a global incident optical beam and the application of distinct back-gate voltages to different devices. The RESET for any desired device can done by setting its gate voltages to zero and illuminating with a global incident optical beam.

Origin of the phenomenon

Photodoping of the graphene channel requires charge transfer from hBN to graphene. The energy corresponding to violet light ($\lambda = 427$ nm) is 2.9 eV, much lower than the band gap of hBN (≈6 eV), precluding photo-excitation of carriers from the valence band of hBN. We also find that the graphene channel remained undoped in a device with only the top hBN flake and without the bottom hBN flake upon using the same protocol described above (Supplementary Note 2). This study confirms that only the bottom hBN was responsible for the photodoping effect. Although the top hBN is not essential for the operation of the device, it is crucial for having a high-quality, low-defect graphene channel with long-term stability.

Based on our observations, we sketch out a possible scenario below that explains all our experimental findings. Figure 4a is a schematic of the energy alignment of the bottom hBN and the graphene without photo-excitation and at $V_g = 0$. Several mid-gap states in hBN can act as electron donors. Of these, the one most relevant for us is the defect state of nitrogen vacancies (marked as $\mathcal{E}_N$ in Fig. 4). This level can have stable charge states of + 1 or 0[38].

A negative gate-voltage $V_g = V_g^*$ dopes the graphene channel with holes and creates an electric field E_{ext} directed from graphene into the hBN (Fig. 4b) leading to band bending. Illuminating the device with violet light excites electrons from $\mathcal{E}_N$ to the conduction band $\mathcal{E}_C$ of hBN. These electrons are funneled to the graphene channel under the influence of the electric field. The holes left at $\mathcal{E}_N$ in the hBN generate an electric field E_i in the direction opposite E_{ext} (Fig. 4c). The electron transfer process continues until the net electric field between graphene and hBN $E_{net} = E_{ext} - E_i$ becomes zero. Simple electrostatics arguments show that the effective number density in graphene becomes zero at this point, which manifests as a shift of the charge neutrality point to V_g^* (Fig. 4d).

On reducing V_g to zero, graphene draws negative charges from the metal contacts, making the net device charge neutral (Fig. 4e). This charge configuration generates an electric field E_i directed from the hBN to graphene. The consequent band bending and the fact that $\mathcal{E}_N > \mathcal{E}_D$ forbids electron transfer back from graphene to the hBN; graphene remains negatively charged with the Dirac point at $V_g = V_g^*$, and hBN is positively charged (Fig. 4e). This constitutes the SET protocol. The energy barrier to back-transfer electrons from graphene to hBN explains the long-term charge retention in graphene after the photodoping is completed.

Exposing the device to light with $V_g^* = 0$ V erases the doping, bringing the graphene's Dirac point back to $V_g = 0$ V. For this to happen, excess electrons need to be removed from graphene and transferred back to hBN.

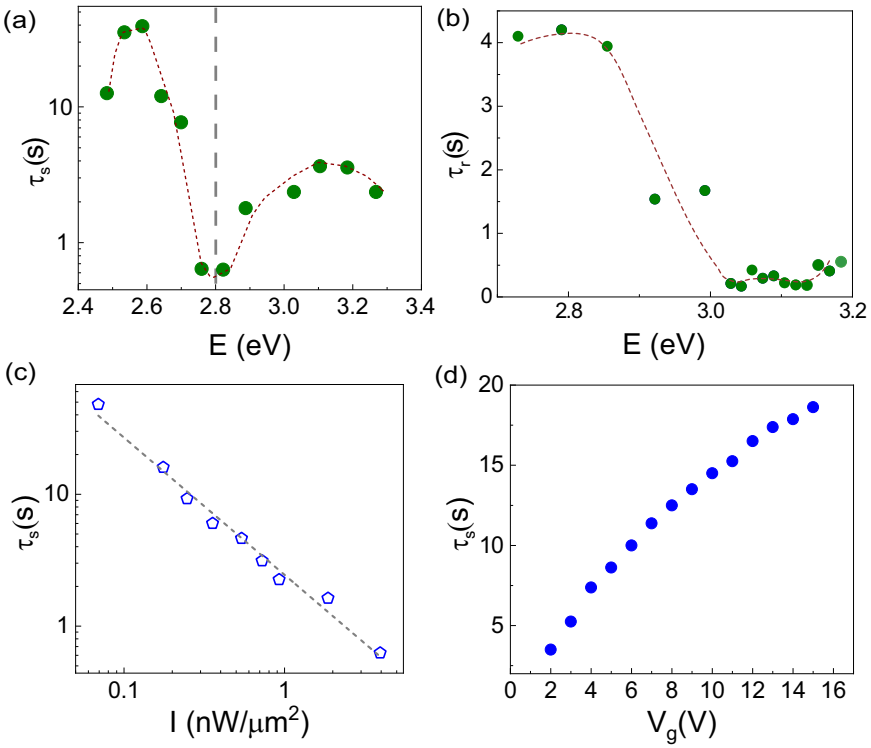

Fig. 5 | Wavelength, power and gate dependence of doping dynamics. a Plot of time constant, τ_s versus the laser photon energy for electron doping. The data were taken at a fixed gate voltage $V_g^* = -3$ V and laser intensity 10^3 Wm^{-2}. The dashed gray line marks $\mathcal{E}_N$. The dotted red line is a guide to the eye. **b** Plot of time constant, τ_r versus the laser photon energy for hole doping. The data were taken at a fixed gate voltage $V_g^* = 3$ V and laser intensity 10^5 Wm^{-2}. The dotted red line is a guide to the eye. **c** Log-log plot of time constant τ_s versus the intensity of incident light. The data were taken at $V_g^* = -5$ V and $\lambda = 427$ nm using LED. The open symbols are the measured data points, and the dashed gray line is a linear fit to the data. **d** Plot of τ_s versus the V_g^* for electron doping. The data was taken for $\lambda = 427$ nm and $I = 62$ Wm^{-2} using LED.

Note, however, that this process is energetically unfavorable as $\mathcal{E}_N > \mathcal{E}_D$ at the interface. We propose a phenomenological scenario in which this RESET process is a two-step process involving (1) the transfer of electrons from the valence band of hBN to its mid-gap states due to optical excitation and (2) subsequent electron transfer from graphene to the empty valence band states of hBN due to electric field (Fig. 4f). Consequently, the RESET process (involving electron transfer from graphene to hBN) is much slower than the SET process for electron doping. Device-level simulations are required to verify if the above scenario correctly captures the doping erasure process.

To experimentally verify the scenario proposed above, we used a tunable pulse laser to study the wavelength dependence of the 'SET' time τ_s. Figure 5a plots τ_s versus the laser photon energy for a constant laser intensity and $V_g^* = -3$ V. It shows a minimum centered around $E = 2.8$ eV. This photon energy corresponds to the optical absorption by valence nitrogen defect in hBN '$\mathcal{E}_N$,' leading credence to our understanding of the photodoping process[37]. The wavelength dependence of the time required for the 'RESET' τ_r is shown in Fig. 5b. In contrast to the SET process, τ_r reaches its minimum value at around $E = 3.2$ eV; this value matches exactly $\mathcal{E}_N - \mathcal{E}_V$; the energy required to excite charge carriers from the valence band to the nitrogen-vacancy state.

We note that the optical power used for the RESET process is higher than that used during the SET process. Thus, one must consider the possibility of the formation of defect states in the hBN during this process. We rule out this scenario by noting the lack of long-term resistance drift, as seen from Fig. 2. We have also considered the possibility of the reversible creation of additional mid-gap states but ruled them out from energetic consideration. The maximum used power for the optical measurements was 10^5 Wm^{-2}, which is significantly lower than the reported power needed to create defects in hBN[46–48].

Figure 5c shows the dependence of τ_s on the intensity of the light, I at a fixed V_g^* and $\lambda = 427$ nm. We find that $\tau_s \propto I^{-1}$. This dependence is understandable, as an increase in the intensity of photons leads to more free charges being produced in hBN, reducing the time taken to dope (see Supplementary Note 1 for detailed derivation). For measurements performed at a fixed intensity of light, the time constant to dope should increase with an increase in the magnitude of V_g^* (equivalently, of E_{ext}); measurements confirm this (Fig. 5d) (See Supplementary Note 1 for detailed derivation).

To summarize, we demonstrate a reversible control of the Dirac point in the graphene-hBN heterostructure to encode the resistance values via a combined optical-electrical stimulus. The device's resistance can be modified by varying the gate voltage in the presence of an optical incident power or by fixing the gate voltage and illuminating it with multiple optical pulses. The switching time can be tuned by the incidence light wavelength (Fig. 5a), light intensity (Fig. 5c), or the gate voltage (Fig. 5d) providing tremendous tunability of the properties of the device. The time taken to electron dope is much less compared to hole doping for a fixed power and gate voltage, and further experiments need to be done to make them comparable. It should be possible to control the switching time by modifying the defect density in hBN using electron irradiation or annealing processes. The ability to photoelectrically SET, READ, and RESET multiple stable and non-volatile resistance states of the device makes it ideal for use as a memristor.

Methods

Device fabrication

The devices were fabricated using the dry transfer technique[49]. Single-layer graphene (SLG) and hexagonal boron nitride (hBN) flakes were mechanically exfoliated onto a Si/SiO_2 substrates. The hBN flakes had a thickness of 25–30 nm. Electron beam lithography was used to define electrical contacts. This was followed by etching with a mixture of CHF_3 (40 sscm) and O_2 (10 sscm). The metallization was done with Cr/Au (5 nm/60 nm) to form the 1D electrical contacts with SLG.

Measurements

All electrical transport measurements were performed at room temperature using a low-frequency AC measurement technique. For low-temperature measurements, the sample was cooled down in a cryostat to 4.7 K. For optoelectronic measurements, the sample was illuminated using either an LED of wavelength, $\lambda = 427$ nm, or a Ti Sapphire pulsed laser (80 MHz repetition rate, 100 fs pulse width).

Data availability

The authors declare that the data supporting the findings of this study are available within the main text and its supplementary Information. Other relevant data are available from the corresponding author upon request.

Received: 17 July 2024; Accepted: 19 September 2024;
Published online: 29 October 2024

References

1. Sangwan, V. K. & Hersam, M. C. Neuromorphic nanoelectronic materials. *Nat. Nanotechnol.* **15**, 517–528 (2020).
2. Walters, B., Jacob, M. V., Amirsoleimani, A. & Rahimi Azghadi, M. A review of graphene-based memristive neuromorphic devices and circuits. *Adv. Intell. Syst.* **5**, 2300136 (2023).
3. Lu, H. et al. Ferroelectric tunnel junctions with graphene electrodes. *Nat. Commun.* **5**, 5518 (2014).
4. Wu, J. et al. High tunnelling electroresistance in a ferroelectric van der Waals heterojunction via giant barrier height modulation. *Nat. Electron.* **3**, 466–472 (2020).
5. Yan, X. et al. Moiré synaptic transistor with room-temperature neuromorphic functionality. *Nature* **624**, 551–556 (2023).
6. Liu, H., Liu, Y. & Zhu, D. Chemical doping of graphene. *J. Mater. Chem.* **21**, 3335–3345 (2011).
7. Wehling, T. O. et al. Molecular doping of graphene. *Nano Lett.* **8**, 173–177 (2008).
8. Jung, N. et al. Charge transfer chemical doping of few layer graphenes: charge distribution and band gap formation. *Nano Lett.* **9**, 4133–4137 (2009).
9. Bruna, M. & Borini, S. Observation of Raman $ G $-band splitting in top-doped few-layer graphene. *Phys. Rev. B* **81**, 125421 (2010).
10. Zhan, D. et al. FeCl3-based few-layer graphene intercalation compounds: single linear dispersion electronic band structure and strong charge transfer doping. *Adv. Funct. Mater.* **20**, 3504–3509 (2010).
11. Zhao, W., Tan, P. H., Liu, J. & Ferrari, A. C. Intercalation of few-layer graphite flakes with FeCl3: Raman determination of fermi level, layer by layer decoupling, and stability. *J. Am. Chem. Soc.* **133**, 5941–5946 (2011).
12. Zhao, W., Tan, P., Zhang, J. & Liu, J. Charge transfer and optical phonon mixing in few-layer graphene chemically doped with sulfuric acid. *Phys. Rev. B* **82**, 245423 (2010).
13. Singh, A. K. et al. Molecular n-doping of chemical vapor deposition grown graphene. *J. Mater. Chem.* **22**, 15168 (2012).
14. Medina, H., Lin, Y.-C., Obergfell, D. & Chiu, P.-W. Tuning of charge densities in graphene by molecule doping. *Adv. Funct. Mater.* **21**, 2687–2692 (2011).
15. Ryu, S. et al. Atmospheric oxygen binding and hole doping in deformed graphene on a SiO2 substrate. *Nano Lett.* **10**, 4944–4951 (2010).
16. Dean, C. R. et al. Boron nitride substrates for high-quality graphene electronics. *Nat. Nanotechnol.* **5**, 722–726 (2010).
17. Das, A. et al. Monitoring dopants by Raman scattering in an electrochemically top-gated graphene transistor. *Nat. Nanotechnol.* **3**, 210–215 (2008).
18. Yan, J., Zhang, Y., Kim, P. & Pinczuk, A. Electric field effect tuning of electron-phonon coupling in graphene. *Phys. Rev. Lett.* **98**, 166802 (2007).
19. Chen, F., Qing, Q., Xia, J., Li, J. & Tao, N. Electrochemical gate-controlled charge transport in graphene in ionic liquid and aqueous solution. *J. Am. Chem. Soc.* **131**, 9908–9909 (2009).
20. Uesugi, E., Goto, H., Eguchi, R., Fujiwara, A. & Kubozono, Y. Electric double-layer capacitance between an ionic liquid and few-layer graphene. *Sci. Rep.* **3**, 1595 (2013).
21. Tiberj, A. et al. Reversible optical doping of graphene. *Sci. Rep.* **3**, 2355 (2013).
22. Aftab, S., Iqbal, M. Z. & Iqbal, M. W. Programmable photo-induced doping in 2D materials. *Adv. Mater. Interfaces* **9**, 2201219 (2022).
23. Neumann, C. et al. Spatial control of laser-induced doping profiles in graphene on hexagonal boron nitride. *ACS Appl. Mater. Interfaces* **8**, 9377–9383 (2016).
24. Ju, L. et al. Photoinduced doping in heterostructures of graphene and boron nitride. *Nat. Nanotechnol.* **9**, 348–352 (2014).
25. Roy, K. et al. Graphene-MoS2 hybrid structures for multifunctional photoresponsive memory devices. *Nat. Nanotechnol.* **8**, 826–830 (2013).
26. Kim, Y. D. et al. Focused-laser-enabled p-n junctions in graphene field-effect transistors. *ACS Nano* **7**, 5850–5857 (2013).
27. Song, S.-B. et al. Deep-ultraviolet electroluminescence and photocurrent generation in graphene/hBN/graphene heterostructures. *Nat. Commun.* **12**, 7134 (2021).
28. Velasco, J. J. et al. Nanoscale control of rewriteable doping patterns in pristine graphene/boron nitride heterostructures. *Nano Lett.* **16**, 1620–1625 (2016).
29. Kim, S. H. et al. Multilevel MoS_2 optical memory with photoresponsive top floating gates. *ACS Appl. Mater. Interfaces* **11**, 25306–25312 (2019).
30. Liu, C.-H., Chang, Y.-C., Norris, T. B. & Zhong, Z. Graphene photodetectors with ultra-broadband and high responsivity at room temperature. *Nat. Nanotechnol.* **9**, 273–278 (2014).
31. Xiang, D. et al. Two-dimensional multibit optoelectronic memory with broadband spectrum distinction. *Nat. Commun.* **9**, 2966 (2018).
32. Tran, M. D. et al. Two-terminal multibit optical memory via van der Waals heterostructure. *Adv. Mater.* **31**, 1807075 (2019).
33. Lee, I. et al. Photoinduced tuning of Schottky barrier height in graphene/MoS2 heterojunction for ultrahigh performance short channel phototransistor. *ACS Nano* **14**, 7574–7580 (2020).
34. Gorecki, J., Apostolopoulos, V., Ou, J.-Y., Mailis, S. & Papasimakis, N. Optical gating of graphene on photoconductive Fe:LiNbO3. *ACS Nano* **12**, 5940–5945 (2018).
35. Seo, B. H., Youn, J. & Shim, M. Direct laser writing of air-stable p-n junctions in graphene. *ACS Nano* **8**, 8831–8836 (2014).
36. Miller, D., Blaikie, A. & Alemán, B. J. Nonvolatile rewritable frequency tuning of a nanoelectromechanical resonator using photoinduced doping. *Nano Lett.* **20**, 2378–2386 (2020).
37. Attaccalite, C., Bockstedte, M., Marini, A., Rubio, A. & Wirtz, L. Coupling of excitons and defect states in boron-nitride nanostructures. *Phys. Rev. B* **83**, 144115 (2011).
38. Weston, L., Wickramaratne, D., Mackoit, M., Alkauskas, A. & Van De Walle, C. G. Native point defects and impurities in hexagonal boron nitride. *Phys. Rev. B* **97**, 214104 (2018).
39. Sajid, A., Reimers, J. R. & Ford, M. J. Defect states in hexagonal boron nitride: assignments of observed properties and prediction of properties relevant to quantum computation. *Phys. Rev. B* **97**, 064101 (2018).
40. Strand, J., Larcher, L. & Shluger, A. L. Properties of intrinsic point defects and dimers in hexagonal boron nitride. *J. Phys. Condens. Matter* **32**, 055706 (2020).
41. Amin, K. R., Nagarajan, R., Pandit, R. & Bid, A. Multifractal conductance fluctuations in high-mobility graphene in the integer quantum hall regime. *Phys. Rev. Lett.* **129**, 186802 (2022).
42. Ducry, F. et al. An ab initio study on resistance switching in hexagonal boron nitride. *npj 2D Mater. Appl.* **6**, 1–10 (2022).
43. Xie, J., Afshari, S. & Sanchez Esqueda, I. Hexagonal boron nitride (h-BN) memristor arrays for analog-based machine learning hardware. *npj 2D Mater. Appl.* **6**, 1–7 (2022).
44. Maier, P. et al. Electro-photo-sensitive memristor for neuromorphic and arithmetic computing. *Phys. Rev. Appl.* **5**, 054011 (2016).
45. Schranghamer, T. F., Oberoi, A. & Das, S. Graphene memristive synapses for high precision neuromorphic computing. *Nat. Commun.* **11**, 5474 (2020).
46. Gan, L. et al. Large-scale, high-yield laser fabrication of bright and pure single-photon emitters at room temperature in hexagonal boron nitride. *ACS Nano* **16**, 14254–14261 (2022).

47. Kianinia, M., White, S., Fröch, J. E., Bradac, C. & Aharonovich, I. Generation of spin defects in hexagonal boron nitride. *ACS Photonics* **7**, 2147–2152 (2020).
48. Yang, Y.-Z. et al. Laser direct writing of visible spin defects in hexagonal boron nitride for applications in spin-based technologies. *ACS Appl. Nano Mater.* **6**, 6407–6414 (2023).
49. Tiwari, P. et al. Observation of the time-reversal symmetric hall effect in graphene-WSe2 heterostructures at room temperature. *Nano Lett.* **23**, 6792–6798 (2023).

Acknowledgements

A.B. acknowledges funding from the Department of Science & Technology FIST program and the U.S. Army DEVCOM Indo-Pacific (Project number: FA5209 22P0166). K.W. and T.T. acknowledge support from JSPS KAKENHI (Grant Numbers 19H05790, 20H00354, and 21H05233). A.S. acknowledges funding from the Indian Institute of Science start-up grant, DST Nanomission CONCEPT (Consortium for Collective and Engineered Phenomena in Topology) grant and project MoE-STARS-2/2023-0265. M.M. acknowledges the Prime Minister's Research Fellowship (PMRF).

Author contributions

H.K.M, M.M., V.S., A.S. and A.B. conceptualized the study, performed the measurements, and analyzed the data. K.W. and T.T. grew the hBN single crystals. All the authors contributed to preparing the manuscript.

Competing interests

The authors declare no competing interests.

Additional information

Supplementary information The online version contains supplementary material available at https://doi.org/10.1038/s41699-024-00503-7.

Correspondence and requests for materials should be addressed to Akshay Singh or Aveek Bid.